Novel Carbon-Encapsulated Porous SnO₂ Anode for Lithium-Ion Batteries with Much Improved Cyclic Stability

Bin Huang, Xinhai Li,* Yi Pei, Shuang Li, Xi Cao, Robert C. Massé, and Guozhong Cao*

Porous SnO$_2$ submicrocubes (SMCs) are synthesized by annealing and HNO$_3$ etching of CoSn(OH)$_6$ SMCs. Bare SnO$_2$ SMCs, as well as bare commercial SnO$_2$ nanoparticles (NPs), show very high initial discharge capacity when used as anode material for lithium-ion batteries. However, during the following cycles most of the Li ions previously inserted cannot be extracted, resulting in considerable irreversibility. Porous SnO$_2$ cubes have been proven to possess better electrochemical performance than the dense nanoparticles. After being encapsulated by carbon shell, the obtained yolk–shell SnO$_2$ SMCs@C exhibits significantly enhanced reversibility for lithium-ions storage. The reversibility of the conversion between SnO$_2$ and Sn, which is largely responsible for the enhanced capacity, has been discussed. The porous SnO$_2$ SMCs@C shows much increased capacity and cycling stability, demonstrating that the porous SnO$_2$ core is essential for better lithium-ion storage performance. The strategy introduced in this paper can be used as a versatile way to fabrication of various metal-oxide-based composites.

1. Introduction

The large-scale usage of clean energy sources, such as solar, tide, and wind, has attracted worldwide attention. However, effective storage of such renewable and intermittent energy is one of the key factors determining the utilization of clean energy in our modern society.[1,2] Lithium-ion batteries (LIBs) have been used as the most leading power source for portable electronics so far, as they have relatively high energy density, long lifespan, and low self-discharge.[3] Great efforts are being made to further enhance the electrochemical performance of LIBs, so as to meet the ever-growing demand in large-scale applications, especially in transportation sector.[4,5] Novel electrode materials with high energy density and long-term cyclic stability are still highly desired.[6] For instance, the most common graphite anodes have a theoretical capacity of 372 mAh g^{-1}, which is much lower than some transitional metal oxides anodes.[2,4,7]

SnO$_2$, as a semiconductor usually used in gas sensors, possesses a theoretical capacity of 782 mAh g^{-1} for lithium-ions insertion, which is more than twice as high as that of commercial graphite.[8–13] However, Li$^+$ insertion/extraction will lead to significant volume expansion/contraction ($\approx$300%), resulting in pulverization of SnO$_2$ particles and abrupt capacity fading.[8,14] The continual pulverization caused by volume changes during successive charge–discharge cycles will not only insulate some electrochemical active particles from the current collector but also continually facilitate unwanted side reactions between the newly exposed particle surface and electrolyte, thus continually making unnecessary solid-electrolyte interface (SEI).[15] Many strategies have been proposed and investigated to circumvent this problem.[12,13,16–20] For instance, reducing the particle size to nanoscale has been found to alleviate the volume variation,[13,20] and hollow structures could provide vacant kernel to sustain the volume expansion.[18,19] Carbon encapsulation

B. Huang, Y. Pei, S. Li, X. Cao, R. C. Massé, Prof. G. Cao
Department of Materials Science and Engineering
University of Washington
Seattle, WA 98195, USA
E-mail: gzcao@u.washington.edu

B. Huang, Prof. X. Li
School of Metallurgy and Environment
Central South University
Changsha, Hunan 410083, China
E-mail: xinhaili_csu@126.com

of nanostructured or hollow SnO_2 would further improve the electrochemical properties since carbon shell can more or less restrict the mechanical strain and enhance the electrical conductivity.[12,16,17] And from this point of view, some other carbon-containing composites such as SnO_2 with carbon nanotubes (CNTs)[10,21] and SnO_2 with graphene[11] also demonstrated significantly improved performance.

This paper introduces a carbon-encapsulated porous SnO_2 submicrocubes (SMCs) yolk–shell structure (SnO_2 SMCs@C), in which a porous SnO_2 SMC forms a core with a carbon shell separated with a void space. This work was largely inspired by Wang's work,[16] in which they introduced an interesting SnO_2@C yolk–shell structure composed of hollow SnO_2 nanosphere and carbon shell. However, the structure introduced by this work has not been reported before. The porous SnO_2 core would provide plenty cavities or void space to accommodate volume expansion with minimal stress gradient induced by the volume change during the charge/discharge cycles. Moreover, in general, porous structures usually have higher mean density than hollow structures, since there is nothing but void space inside the hollow structures. The space between the porous SnO_2 core and the carbon shell provides sufficient void space for buffering the volume variation of SnO_2 core, thus rendering a very stable microstructure of the electrodes, as the individual yolk–shell structure retains its morphologies during the cycles. The outer carbon shell would also facilitate the electronic conduction. Owing to the advantages of such unique structure, the SnO_2 SMCs@C composite demonstrated excellent electrochemical performance in LIBs, and the relationship between the microstructure and the electrochemical properties of porous SnO_2 carbon yolk–shell composites has been elaborated.

2. Results and Discussion

The porous SnO_2 SMCs were presynthesized by annealing and HNO_3 etching of $CoSn(OH)_6$ SMCs, which were obtained by a simple wet-chemical process (detailed synthetic method is given in the Experimental Section). **Figure 1**a shows the X-ray diffraction (XRD) pattern of the $CoSn(OH)_6$ SMCs, All the peaks can be indexed to $CoSn(OH)_6$ (JCPDS Card No. 13-0356), and no other impurities are observed. The corresponding scanning electron microscope (SEM) image is shown in Figure 1c. As we can see the as-prepared $CoSn(OH)_6$ has smooth cubic morphology with particle size about 200–300 nm. Figure 1b shows the XRD pattern of the compound which was directly obtained by annealing the $CoSn(OH)_6$ at 700 °C in air. As can be seen, the $CoSn(OH)_6$ is converted to a mixture of SnO_2 and Co_3O_4 after thermal treatment. However, the cubic shape is preserved and the only obvious change is that the corners become a little rounded and the surface becomes rough and porous (Figure 1d). This is due to the dehydration of $CoSn(OH)_6$ and the phase segregation while SnO_2 and Co_3O_4 is forming. From the cubic-shaped SnO_2/Co_3O_4 composite we can easily obtain the porous cubic SnO_2 by HNO_3 treatment since SnO_2 cannot be dissolved in HNO_3 solution. Furthermore, after Co_3O_4 is etched away, a fixed amount of pores can be established, which can facilitate the access of electrolyte to the interior of the SnO_2 cubes.

Subsequently the obtained-porous SnO_2 SMCs were successively coated by SiO_2 and resorcinol-formaldehyde (RF) resin using Stober process,[22] followed by carbonization. Finally, the SiO_2 between the SnO_2 core and carbon shell was removed by HF solution for making void space. The synthetic
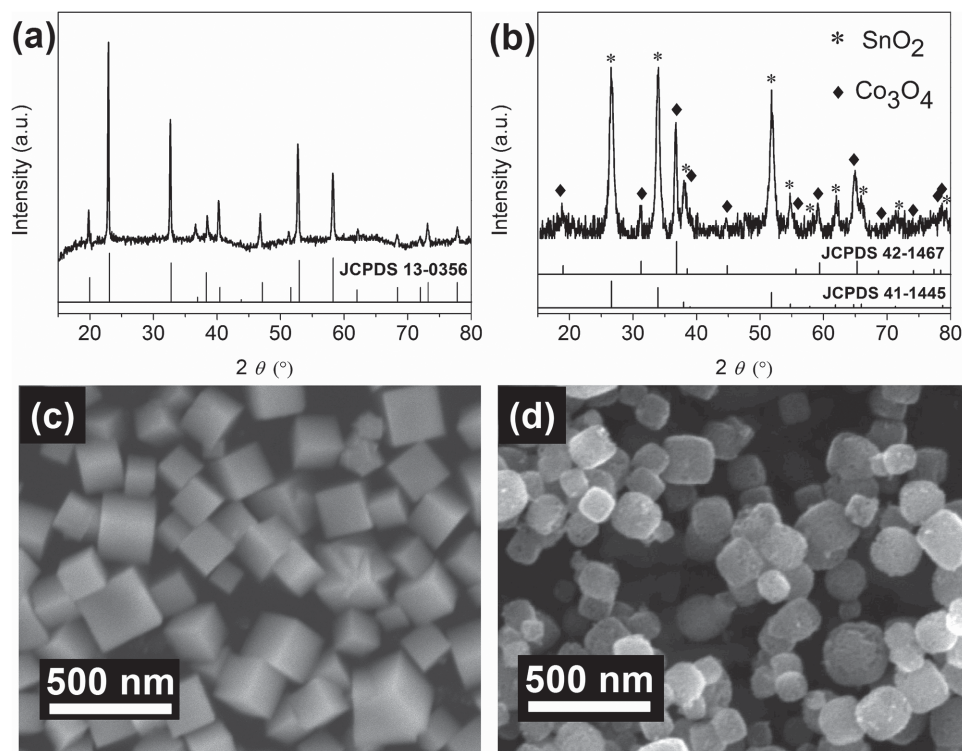
Figure 1. XRD patterns and SEM images of $CoSn(OH)_6$ (a,c), and its derivative (b,d), after being annealed at 700 °C in air for 5 h.
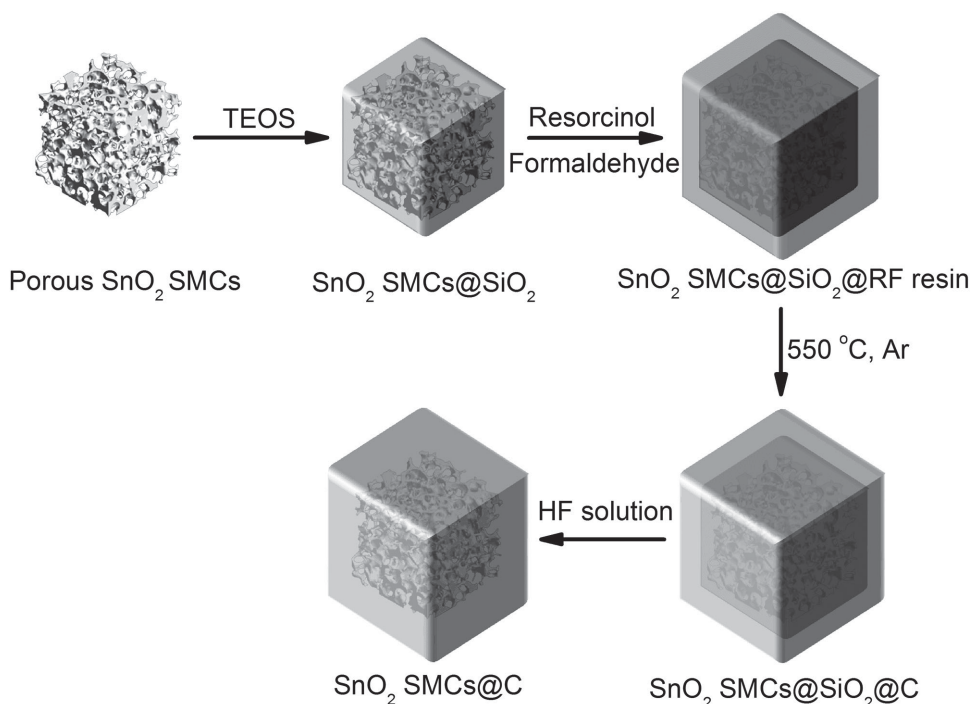
Figure 2. Schematic illustrating the multiple steps applied for the synthesis and formation of SnO$_2$ SMCs@C yolk–shell structure.

procedures described above can be schematically illustrated by **Figure 2**.

Figure 3a shows SEM image of the as-prepared SnO$_2$ SMCs. It can be seen that the porous cubes are around 200–300 nm in edge length. Figure 3b shows SEM image of the carbon-encapsulated SnO$_2$ SMCs. The SnO$_2$ SMCs are individually and completely encapsulated by carbon, and the size of the SnO$_2$ SMCs@C is about 400–500 nm. It also should be noted that between the SnO$_2$ core and the carbon shell there is noticeable vacancy which can buffer the volume expansion for the SnO$_2$ core during charge–discharge cycles. Moreover, the porosity of the SnO$_2$ cubes is not only able to provide space for the volume expansion, but also beneficial to the electrochemical reactivity. In order to observe the interior structure of the SnO$_2$ SMCs@C more clearly, transmission electron microscope (TEM) measurement was also implemented. The results are shown in Figure 3c,d. From the TEM images we can clearly see the porous SnO$_2$ core and the complete carbon shell with a thickness of about 8–10 nm. Moreover, it can be seen that the average distance from the internal surface of the shell to the outer surface of the core is about several tens of nanometers. Figure 3e shows that the porous SnO$_2$ core is composed of well-crystallized SnO$_2$ nanoparticles with a diameter of about 12 nm.

Energy dispersive X-ray spectrometry (EDS) was used to detect the elements in the as-prepared sample. The results are shown in **Figure 4**. The EDS spectrum (Figure 4a) was collected from the region marked by the white rectangle frame in Figure 4b, indicating that no Co or Si is detected. Figure 4d shows the signals collected along the scanning track marked by the black arrow in Figure 4c, and Figure 4e displays the mapping signals obtained from the region bounded by the dashed box in Figure 4c. The linear scanning and mapping

only detect Sn and O signals on the porous SnO$_2$ core (carbon and copper signals were not saved since the sample was loaded on a carbon coated copper grid). Therefore, it can be proved that Co and Si are thoroughly removed during the synthesis. The existence of carbon in SnO$_2$ SMCs@C was proven by Raman spectra as shown in **Figure 5**, in which the SnO$_2$ SMCs@C showed two broad peaks located at 1363 and 1594 cm^{-1}, which are assigned to D and G bands of carbon, respectively.[23] The Raman spectrum of SnO$_2$ SMCs@C also revealed amorphous nature of the carbon shell.[24]

Figure 6a provides the results of nitrogen adsorption measurement implemented on the bare SnO$_2$ SMCs sample. The SnO$_2$ SMCs exhibits a type V isotherm curve (the inset) which suggests its mesoporous structure. The pore size distribution curve indicates that the sample has a relatively narrow pore size distribution around 20 nm. Additionally, the pore volume is calculated to be 0.32 cm^3 g^{-1}. By taking the advantage of the porosity, electrolyte can easily penetrate into the interior of the SnO$_2$ cubes, facilitating the electrochemical reactions occurred at the interface between SnO$_2$ and electrolyte. Moreover, a specific high surface area can also be expected. According to the Brunauer–Emmett–Teller (BET) computational method, the specific surface area of the SnO$_2$ SMCs is 107 m^2 g^{-1}, which is slightly larger than that of the commercial SnO$_2$ nanoparticles (Sigma-Aldrich, <100 nm in particle size) (98 m^2 g^{-1}, the nitrogen adsorption measurement result of the SnO$_2$ NPs is given in Figure S1 in the Supporting Information). In order to quantitatively determine the carbon content for the SnO$_2$ SMCs@C, thermogravimetric analysis (TGA) was implemented (Figure 6b). The TGA curve indicates that the carbon content in the SnO$_2$ SMCs@C is about 29 wt%. In our experiment, we prepared three samples with different carbon content (21, 29, and
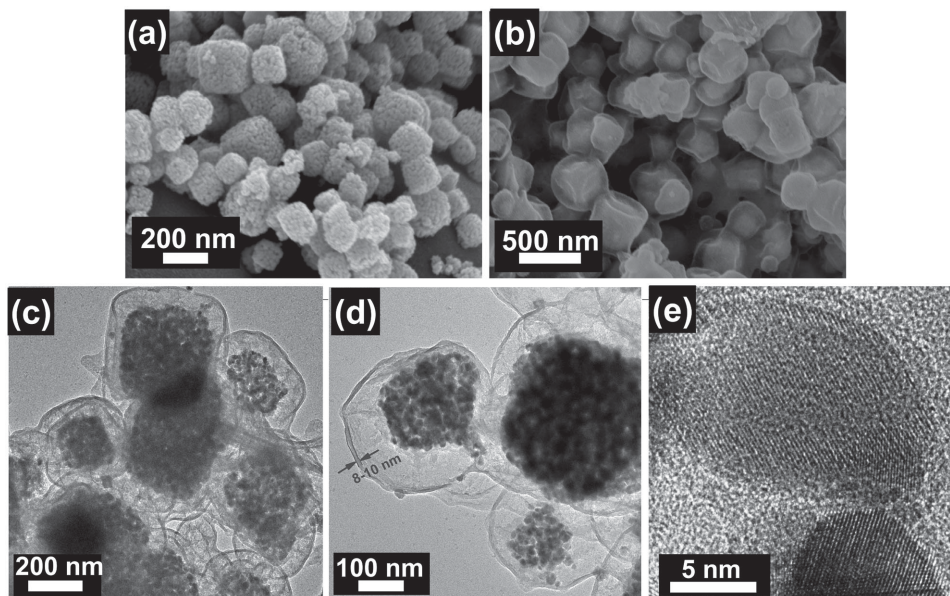
Figure 3. SEM images of a) bare SnO$_2$ SMCs, and b) SnO$_2$ SMCs@C. c,d) TEM images of SnO$_2$ SMCs@C. e) high-resolution TEM image of SnO$_2$ SMCs@C.

42 wt%, which were all determined by TGA; see Figure S2 in the Supporting Information), finding that the sample with 29 wt% carbon content exhibited the best electrochemical performance (Figure S3, Supporting Information). Thus in this paper the sample with 29 wt% carbon was chosen for further study.

The as-prepared SnO$_2$ SMCs@C with 29% carbon content was electrochemically tested in a CR 2016 coin-type half-cell. For comparison, bare commercial SnO$_2$ NPs, the bare porous SnO$_2$ SMCs and carbon-encapsulated SnO$_2$ NPs (SnO$_2$ NPs@C) were also electrochemically measured.
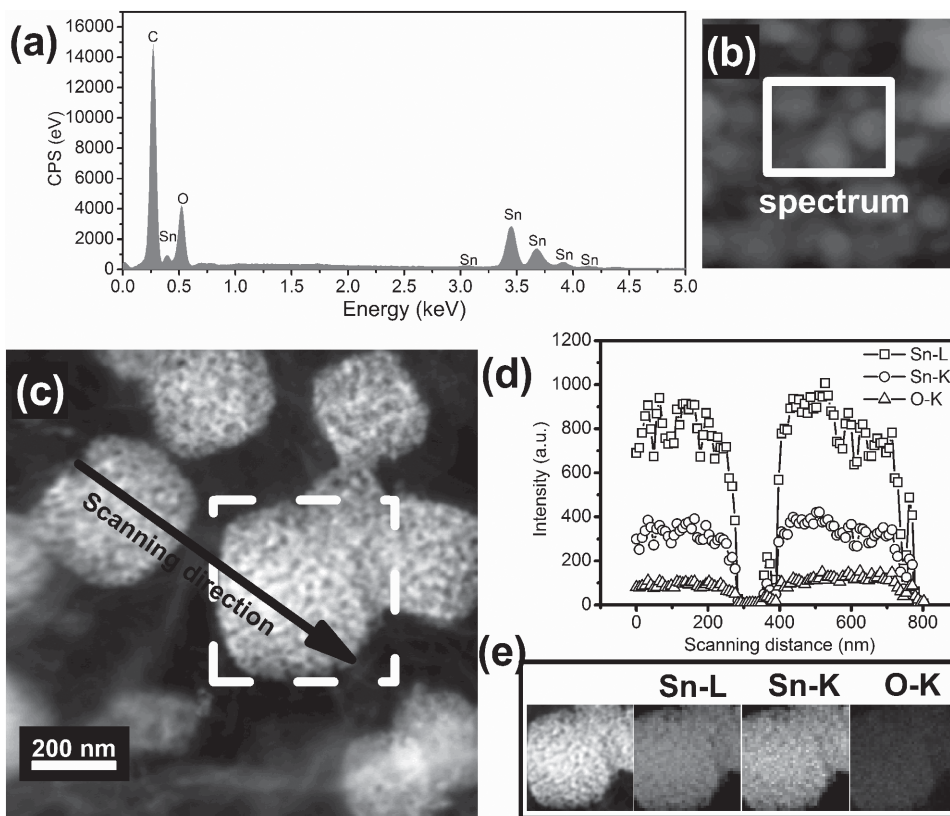

Figure 4. a) EDS spectrum collected from the region bounded by the white box in the SEM image (b). c) TEM image together with EDS linear scanning signals (d) collected along the black arrow, and EDS mappings (e) collected from the region bounded by the dashed box.
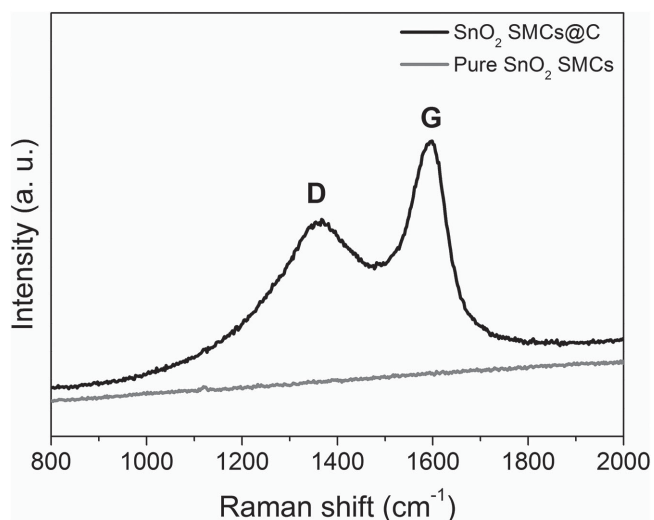
Figure 5. Raman spectra of SnO₂ SMCs@C and bare SnO₂ SMCs.

Figure 7 shows the XRD patterns of the as-prepared SnO₂ SMCs@C, SnO₂ NPs@C, bare SnO₂ SMCs, and bare SnO₂ NPs. All the samples have almost the same XRD pattern. The diffraction peaks of each sample can be indexed to rutile SnO₂ (JCPDS Card No. 41-1445); while no peaks of impurities are observed. Additionally, no peaks belonging to carbon are detected, suggesting the amorphous nature of the carbon shell.[25] The crystallite sizes of the bare SnO₂ SMCs and the bare SnO₂ NPs have also been roughly estimated by JADE 9 using their strongest peaks based on the Scherrer equation. The crystallite size of the SnO₂ SMCs is estimated to be about 14 nm, which approximates the value observed by TEM (Figure 3e), while that of the SnO₂ NPs is estimated to be 18 nm. Thus, on average, it is revealed that the porous SnO₂ SMCs have smaller crystallite size than the dense SnO₂ NPs.

Figure 8 shows the cyclic voltammetry (CV) curves of the four samples between 0.01 and 2.00 V (vs Li⁺/Li) at a scan rate of 0.1 mV s⁻¹. For comparison, the current axis of each plot has been normalized by the weight of the active material in each cell, and the scales of the axes have been unified. As can be seen, for all the four samples the CV curves roughly exhibit two cathodic and two anodic peaks that can be ascribed to the two electrochemical process described by Equations (1) and (2). Additionally, it is worth noting that the cathodic peaks during the first cycle are significantly higher than those in the

subsequent cycles and their corresponding anodic peaks, especially for the SnO₂ NPs (Figure 8d). It has been recognized that the large cathodic current in the first cycle is largely due to the formation of SEI layer,[8,12,26] which is considered to be essentially irreversible in the subsequent cycles. When encapsulated with carbon, the peak current related to the reversible reactions becomes larger, and the cathodic current during the first cycle becomes weaker, indicating that the capacity loss is suppressed (Figure 8b). Moreover, the increase of the peak intensity at 0.61 V in Figure 8b indicates an activation process in the initial electrochemical reactions as suggested in literature.[27] Compared with SnO₂ NPs, the porous SnO₂ SMCs shows higher intensity peaks in the second and third cycles, indicating relatively higher reactivity and high reversibility (Figure 8c). For the SnO₂ SMCs@C sample (Figure 8a), the cathodic peaks in the first cycle are nearly twice as intense as those in the second and third one. The anodic peaks from the first to third cycle and the cathodic peaks from the second to third cycle almost overlap, indicating excellent cycling stability. Furthermore, for all the samples, the cathodic peaks around 0.6–0.8 V in the first cycle all slightly shift to higher voltage in the second and third cycles, which is a common phenomenon for most conversion anodes,[28] and the decreased current intensity is due to the irreversibility of the reaction described by Equation (1) during charge process[17]

$$SnO_2 + 4Li^+ + 4e^- \leftrightarrow Sn + 2Li_2O \tag{1}$$

$$Sn + xLi^+ + xe^- \leftrightarrow Li_xSn (0 \leq x \leq 4.4) \tag{2}$$
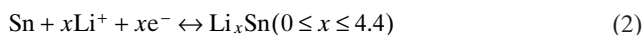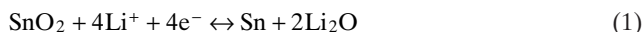
What is noteworthy is that the anodic peak at about 1.29 V for the SnO₂ SMCs@C sample is relatively more obvious and stable than the others. It is proven that the anodic peak around that potential is related to the backward direction of Equation (1).[29–31] That means the metallic Sn comes from SnO₂ will be partially reoxidized to SnO₂, and the Li₂O will be partially decomposed. But the traditional knowledge about Equation (1) is that the conversion from SnO₂ to Sn is irreversible, and the theoretical capacity of SnO₂ (782 mAh g⁻¹) is calculated based on the assumption that Equation (1) is fully irreversible. However, what is interesting is that many researchers found similar results like us. For example, hierarchical mesoporous SnO₂ composed of extremely small primary nanoparticles showed distinct anodic peak around 1.27 V.[31] Many SnO₂/C composites also showed obvious
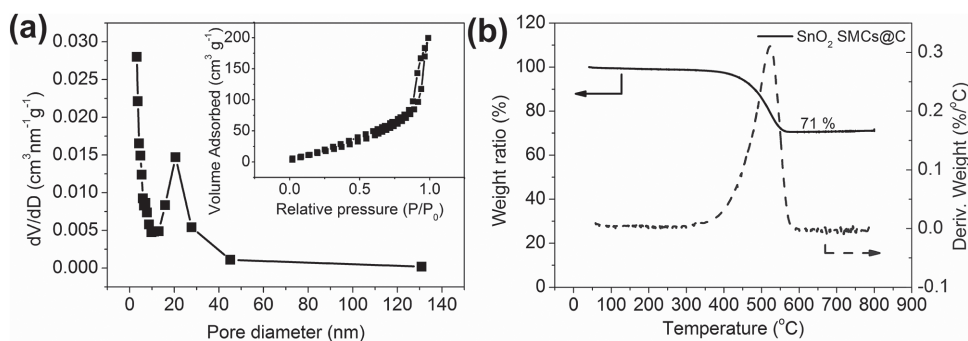

Figure 6. Pore-size distribution of bare SnO₂ SMCs (a) together with the nitrogen adsorption−desorption isotherms (inset) and TGA curve of SnO₂ SMCs@C (b).
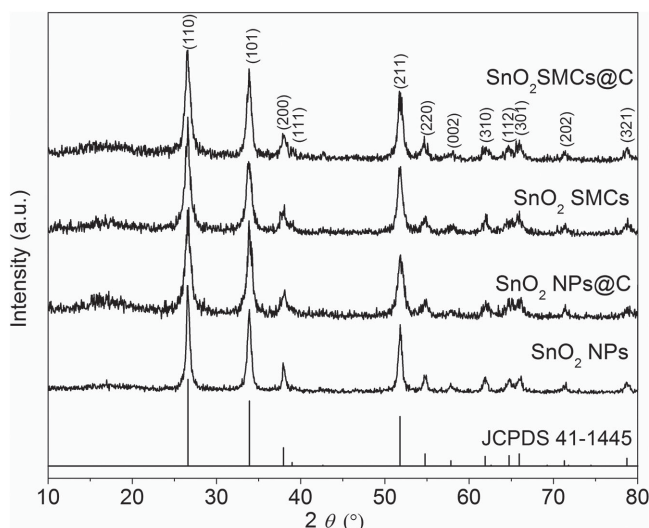
Figure 7. XRD patterns of commercial SnO₂ NPs, SnO₂ NPs@C, SnO₂ SMCs, and SnO₂ SMCs@C.

anodic peaks at that potential.[15,23,31,32] In our experiment, the mesoporous SnO₂ SMCs (Figure 8c), the SnO₂ NPs@C (Figure 8b) and the SnO₂ SMCs@C (Figure 7a) all show the anodic peaks related to the backward direction of Equation (1) in their CV curves. In fact, the bare SnO₂ NPs sample also has that anodic peak around 1.2 V, but too weak to be observed unless in an amplified plot (the inset of Figure 8d). Furthermore, although the bare SnO₂ SMCs shows a peak at 1.23 V (Figure 8c), it decays obviously in the second and third cycles. However, the SnO₂ SMCs@C and SnO₂ NPs@C have more stable anodic peaks at 1.29 and 1.42 V, respectively, suggesting that the carbon shell can enhance and stabilize the reversibility of Equation (1). The difference in the peak

voltages between the two samples could be due to their different polarization. In addition to this, many reported results indicate that some SnO₂-based composites can deliver pretty high actual reversible capacity which is even higher than the recognized theoretical capacity of 782 mAh g⁻¹.[30,32–34] It is probable that the partial reversibility of Equation (1) is responsible for the excess capacity, at least a certain portion of it. For further discussion of the excess capacity, galvanostatic discharge–charge tests are necessary.

Figure 9 shows the voltage-specific capacity plots of first two cycles for the four samples. These tests were carried out at a current density of 50 mA g⁻¹. For the SnO₂ NPs (Figure 9d), the initial discharge capacity is 2130.1 mAh g⁻¹, while the initial charge capacity is 594.7 mAh g⁻¹. Thus the Coulombic efficiency for the first cycle is 27.9%. In the second cycle, it delivers discharge capacity of 618.3 mAh g⁻¹ and charge capacity of 555.1 mAh g⁻¹ with the efficiency of 89.8%. The result shows that the bare SnO₂ NPs has a very high capacity loss during the initial discharge–charge cycle, which is in accord with the CV result (Figure 8d). The substantial irreversible capacity during the first cycle is attributed to the irreversibility of the reaction described by Equation (1) and SEI formation. If Equation (1) is fully irreversible and the Equation (2) is fully reversible, the irreversible capacity consumed by the former will be 711.3 mAh g⁻¹, and the reversible capacity dominated by the latter is 782.4 mAh g⁻¹, which is the recognized theoretical capacity of SnO₂. Thus, based on the above assumption, the theoretical Coulombic efficiency of SnO₂ during the first lithiation/delithiation cycle should be 52.4%. In fact, however, the formation of SEI layer is inevitable and it also leads to considerable irreversible capacity in the first cycle or first several cycles. The formation of SEI layer, coupled with the irreversibility of the reaction described by Equation (1), leads to the large initial capacity loss for the bare SnO₂ NPs sample.
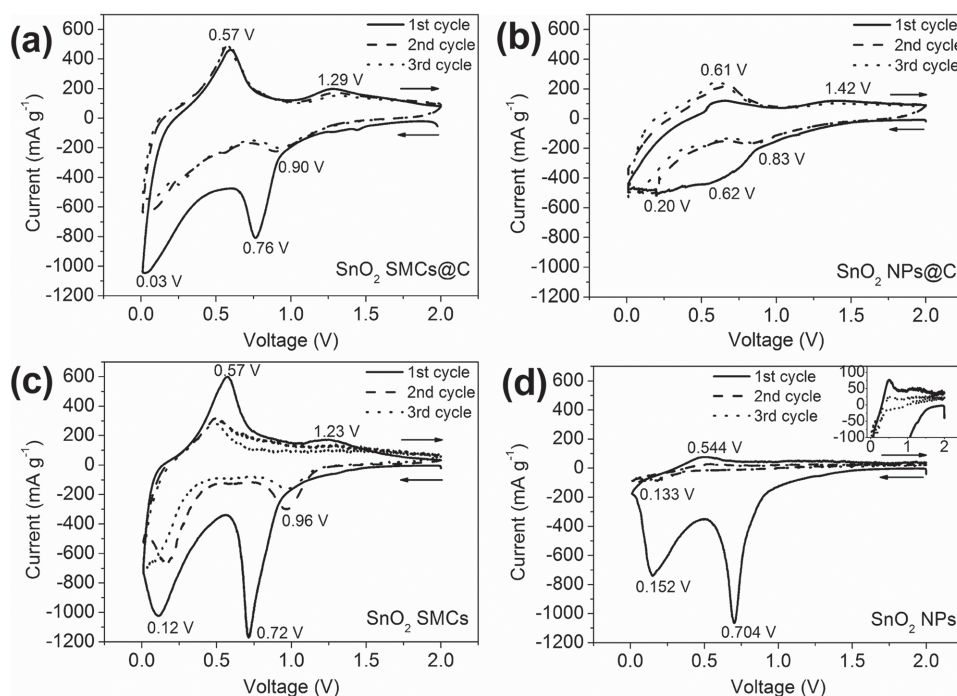

Figure 8. CV curves of SnO₂ SMCs@C (a), SnO₂ NPs@C (b), SnO₂ SMCs (c), and SnO₂ NPs (d).
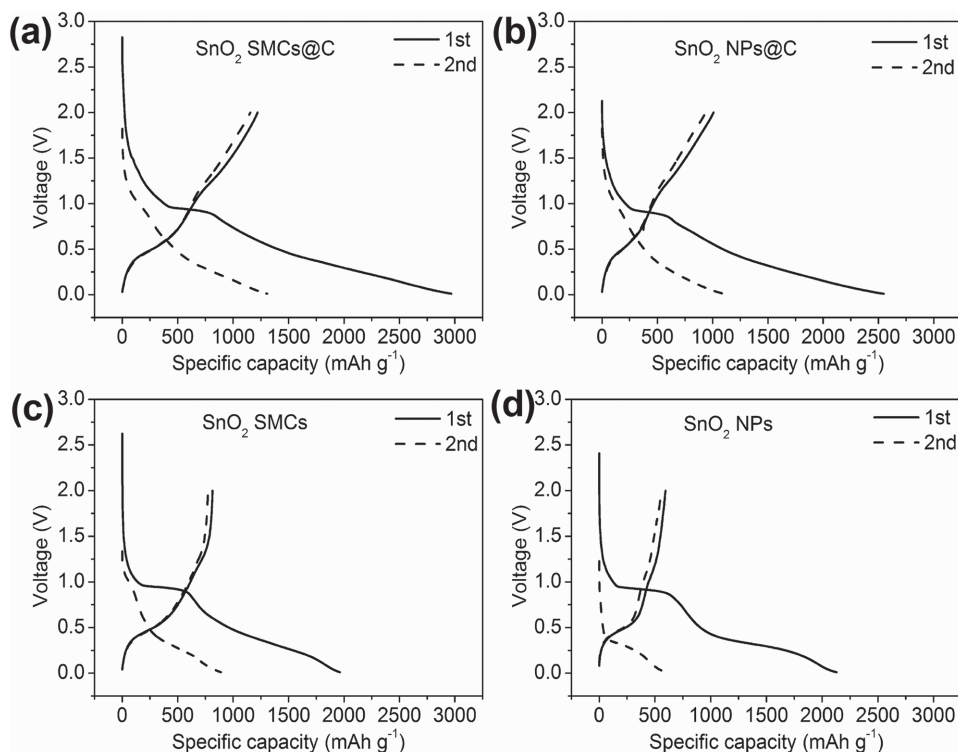
Figure 9. Discharge–charge curves of SnO$_2$ SMCs@C (a), SnO$_2$ NPs@C (b), SnO$_2$ SMCs (c), and SnO$_2$ NPs (d) in their first and second cycles.

By contrast, the bare SnO$_2$ SMCs sample (Figure 9c) exhibits initial discharge capacity of 1963.8 mAh g^{-1} and initial charge capacity of 814.2 mAh g^{-1} with Coulombic efficiency of 41.5%. Therefore, combining the above CV results, it can be concluded that the porous SnO$_2$ exhibits higher capacity and lower irreversibility than the plain dense SnO$_2$ nanoparticles. One possible reason for the enhancement of reversible capacity and Coulombic efficiency is the increased reversibility of Equation (1). When encapsulated by carbon, the SnO$_2$ NPs@C (Figure 9b) delivers initial discharge and charge capacities of 2546.9 and 1008.5 mAh g^{-1}, respectively, with the Coulombic efficiency of 39.6%, while the SnO$_2$ SMCs@C (Figure 9a) has initial discharge and charge capacities of 2969.1 and 1220.3 mAh g^{-1}, with the Coulombic efficiency of 41.1% (The capacities are based on the total weight of the SnO$_2$/carbon composites). As discussed above, carbon-supported SnO$_2$ composites are usually reported to exhibit much enhanced capacity which is even higher than the theoretical capacity of pure SnO$_2$ due to the reversibility of Equation (1). Moreover, the decomposition of electrolyte in low-potential region and the simple adsorption of Li$^+$ on the surface of the supporting carbon matrix are also considered as the causes of the excess capacity.[33,35]

In order to further investigate the cycling stability of the four samples, they were cycled between 0.01 and 2.00 V at a current density of 50 mA g^{-1}. The results are shown in **Figure 10**. As can be seen, the two bare SnO$_2$ samples exhibit faster capacity decay in the first 12 cycles. Then their capacities become more stable. Like the results reported by some other groups,[13,16,18,36] bare SnO$_2$ materials always undergo rapid capacity fading during the first several or tens of cycles. That is the main barrier to the practical application of SnO$_2$. By

contrast, the carbon-encapsulated samples, SnO$_2$ NPs@C and SnO$_2$ SMCs@C, have remarkably enhanced stabilities during discharge–charge cycles. For the SnO$_2$ NPs@C, the charge capacities in the first and the 120th cycle are 1008.5 and 635.0 mAh g^{-1}, respectively, thus the capacity retention is 63.0%; for the SnO$_2$ SMCs@C, the charge capacities in the first and the 120th cycle are 1220.3 and 870.9 mAh g^{-1}, respectively, with the retention of 71.4%. The complete carbon enclosure and the void space between the core and shell can physically restrict the SnO$_2$ core and buffer its volume expansion, preventing it from pulverization and detaching from the current collector. That is beneficial to maintain the high capacity during discharge–charge cycles. Therefore, our treatment
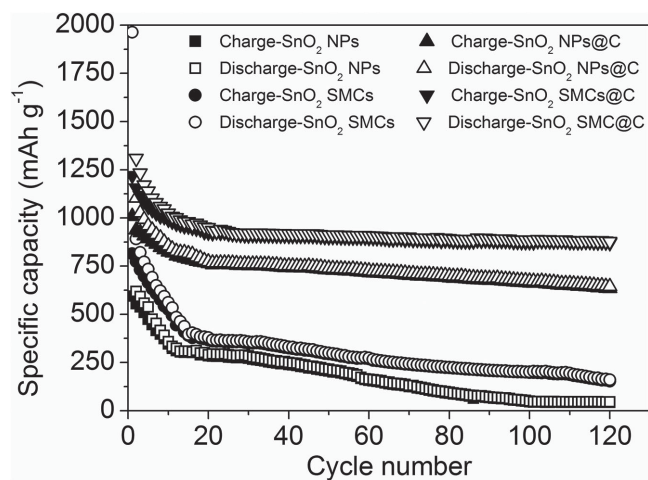

Figure 10. Cycling performances of SnO$_2$ NPs, SnO$_2$ NPs@C, SnO$_2$ SMCs, and SnO$_2$ SMCs@C at a current density of 50 mA g^{-1}.
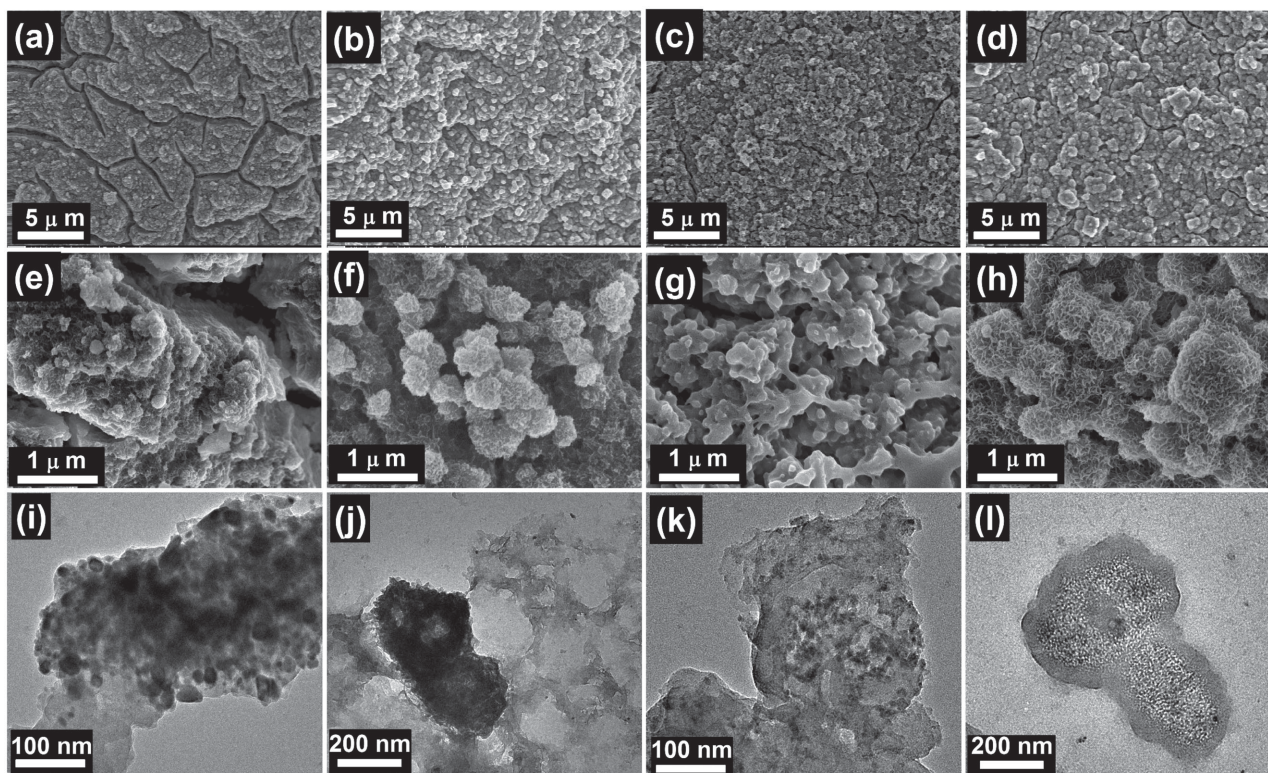
Figure 11. SEM images of SnO₂ NPs (a,e), SnO₂ SMCs (b,f), SnO₂ NPs@C (c,g), and SnO₂ SMCs@C (d,h), together with the corresponding TEM images (i–l).

can significantly enhance the electrochemical performance of SnO₂ materials, making them to be more promising anode materials for LIBs.

To inspect the microstructure of the materials after cycling, the four cells after 120 cycles were disassembled, and the electrodes were rinsed by dimethyl carbonate (DMC) and dried, followed by SEM and TEM tests. For SEM tests, the electrodes were directly observed without any treatment; for TEM tests, the active materials were scraped from electrodes and dispersed in ethanol by ultrasound before testing. The results are given in **Figure 11**. As can be seen, the SnO₂ NPs electrode (Figure 11a) shows severe cracks which are hundreds of nanometers in width. Figure 11i shows that the nanoparticles tend to aggregate into clusters after cycling. There are also many cracks on the electrode loaded with SnO₂ SMCs (Figure 11b). However, the cracks are much narrower, and every single cube is discernible (Figure 11f,j), indicating that the porous structure can relieve the electrode cracking resulting from the volume changes. For the electrodes loaded with SnO₂ NPs@C and SnO₂ SMCs@C (Figure 11c,d), the cracks are fewer than the two bare samples. From Figure 11k we can see that the SnO₂ nanoparticles are not aggregated due to the isolation by carbon. Figure 11l shows the SnO₂ SMCs@C after cycles, it is clearly seen that the carbon shell remains intact after cycling.

To further study the transport kinetics of electrons and ions facilitated by the unique yolk–shell structure, electrochemical impedance spectroscopy was carried out on all samples after 120 cycles. Before the measurements, all of the batteries were charged to 1.0 V for obtaining an iden-

tical status. The data were collected from 100 kHz to 10 mHz. The results are given in **Figure 12**. The high-frequency and medium-frequency semicircles reflect resistances of surface film (R_{sf}) and charge-transfer (R_{ct}), respectively.[37] It can be seen that the bare SnO₂ NPs has the largest R_{sf} and R_{ct} values (5079 and 4450 Ω), which are calculated using the equivalent circuit shown in the inset of Figure 11a. Those values of SnO₂ SMCs are obviously lower (2892 and 2518 Ω), indicating the porous structure is superior to the dense nanoparticles in charge transfer. By contrast, the two carbon-encapsulated samples exhibit much lower impedances, indicating much improved charge transfer kinetics. The R_{sf} and R_{ct} of SnO₂ NPs@C are 245 and 133 Ω, while those values of SnO₂ SMCs@C are 238 and 76 Ω, respectively.

In the following we will further compare the SnO₂ SMCs@C and SnO₂ NPs@C in rate capability and long-term cycling.

Figure 13 shows the rate capabilities of SnO₂ SMCs@C and SnO₂ NPs@C, together with successive cycling tests. In this paper, 1 C is denoted as 500 mA g⁻¹. During the first ten cycles at 0.1 C, both of the two samples show capacity decay and Coulombic efficiency increase, in accord with the results shown in Figure 10. After that, both of them exhibit decent performances in the subsequent rate tests. At 5 C rate, the SnO₂ NPs@C delivers an average charge and discharge capacities of 405.0 and 409.6 mAh g⁻¹. For the SnO₂ SMCs@C, it has an average charge and discharge capacities of 424.9 and 431.1 mAh g⁻¹. After that, the capacities of the two samples can recover to higher values as the current densities reverse back gradually. For instance, by the end of the rate tests stage
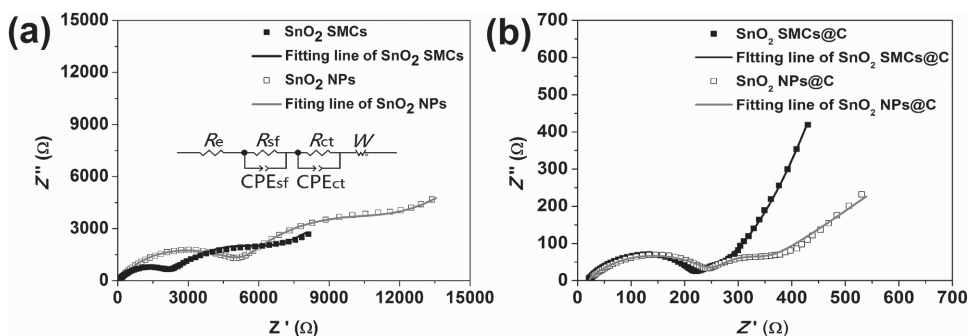
Figure 12. Nyquist plots of the electrodes after 120 cycles. a) Bare SnO$_2$ SMCs and SnO$_2$ NPs and b) carbon-encapsulated SnO$_2$ SMCs@C and SnO$_2$ NPs@C.

(0.1 C), the charge and discharge capacities of SnO$_2$ SMCs@C return to 848.3 and 874.5 mAh g^{-1}, while those of the SnO$_2$ NPs@C return to 679.6 and 699.9 mAh g^{-1}, respectively. It is interesting that the capacity of SnO$_2$ SMCs@C at 5C rate is close to that of the SnO$_2$ NPs@C, suggesting that they may have similar rate-determining step in the electrochemical reactions under high current density. The exact mechanism is not known at the moment and worthy of further investigation; however, the ion diffusion process may become more predominant at high current density. Similar results are also reported in literatures.[27,38] Subsequently the samples are cycled at a constant current density of 1 C for 200 cycles. At the beginning of the cycling tests, SnO$_2$ SMCs@C and SnO$_2$ NPs@C exhibit charge capacities of 639.6 and 548.2, respectively. After 200 cycles, the residual capacities of the two samples are 516.0 and 286.2 mAh g^{-1}, and the respective capacity retentions are 80.7% and 52.2%. Therefore, the SnO$_2$ SMCs@C not only exhibits higher capacity for lithium-ion storage but also shows enhanced cycling stability than the SnO$_2$ NPs@C.

3. Conclusions

Novel yolk–shell-structured SnO$_2$ SMCs@C anode material demonstrated superior lithium-ions storage capacity and stability in comparison with dense SnO$_2$ NPs@C. Similarly, porous SnO$_2$ exhibited higher capacity and better stability than dense SnO$_2$ NPs. The much enhanced capacity was found to be relevant to the reversibility of the conversion between SnO$_2$ and Sn, and the enhanced stability was attributed to its

unique microstructure. Not only does the porous core offer void space to buffer the volume expansion of SnO$_2$ (actually Sn) during lithium-ions insertion/extraction but also provides plenty of tunnels allowing electrolyte to enter into the interior of the cubic core. The space between the carbon shell and the core can further tolerate the volume expansion of the SnO$_2$ core. Moreover, the carbon shell plays a major role in improving the conductivity of the material. By taking the advantages of the structural characteristics, the SnO$_2$ SMCs@C can be used as a stable and high-energy anode material for LIBs. Furthermore, the strategy introduced by this paper can be used as a versatile way to fabrication of various metal-oxide-based composites.

4. Experimental Section

Porous SnO$_2$ SMCs Fabrication: The bare SnO$_2$ SMCs were obtained by modifying the method of Huang's work.[39] A typical synthesis procedure was described as follows. SnCl$_4$·5H$_2$O (1 mmol) and NaOH (10 mmol) were separately dissolved in distilled water (100 mL and 5 mL, respectively), followed by mixing them up thoroughly to form a clear solution. Subsequently, Co(NO$_3$)$_2$·6H$_2$O (1 mmol) was dissolved in distilled water (50 mL) and then mixed with the previously obtained solution under magnetic stirring at room temperature for 2 h. After that the obtained pink suspension liquid was stood overnight. Then CoSn(OH)$_6$ powder can be collected by washing, centrifuging and drying. For preparing SnO$_2$, the cubic CoSn(OH)$_6$ was burned at 700 °C in air for 3 h, followed by HNO$_3$ etching (30 mL, 3 M). The etching process was carried out
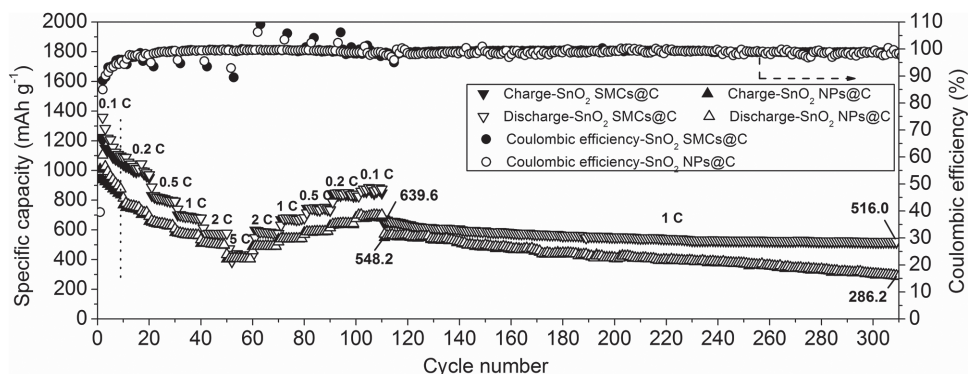

Figure 13. Rate capabilities and 1 C cycling performances of SnO$_2$ NPs@C and SnO$_2$ SMCs@C.

in a Teflon-lined autoclave at 140 °C for 5 h. Finally, the gray-white SnO_2 powder was obtained after washing, centrifuging, and drying.

SnO_2 SMCs@C fabrication: The Stober process was employed to synthesize the final product. The as-prepared porous SnO_2 SMCs (0.2 g) was dispersed in distilled water (5 mL) by ultrasound. Then cetyltrimethyl ammonium bromide (CTAB, 0.1 g) was dissolved in a mixture of distilled water (20 mL), ethanol (10 mL) and 28 wt% ammonium hydroxide solution (0.1 mL) to form a clear solution. Subsequently the above SnO_2 dispersion liquid was added into this solution with stirring, and then tetraethyl orthosilicate (0.39 mL) was added drop by drop. After stirring overnight, the SiO_2-coated SnO_2 (SnO_2 SMCs@SiO_2) was harvested by washing and centrifugation. After that, the SnO_2 SMCs@SiO_2 was dispersed in a solution containing distilled water (15 mL), ethanol (5 mL), CTAB (0.1 g) and 28 wt% ammonium hydroxide solution (0.1 mL) with stirring at 30 °C. Then resorcinol (0.05 g) was added in the solution. After stirring for 30 min, formaldehyde (37%, 0.07 mL) was dropped into the solution. The reaction mixture was stirred for 24 h at 30 °C, followed by hydrothermally treating at 100 °C for another 24 h. Afterwards, the SnO_2 SMCs@SiO_2@RF-resin can be obtained by washing and centrifugation. Finally, the SnO_2 SMCs@SiO_2@RF-resin was heated at 550 °C under Ar flow, and then washed with an HF solution (2 M) to obtain SnO_2 SMC_2@C. SnO_2 NP@C was also prepared by the same process except for using commercial SnO_2 NPs instead of the SnO_2 SMCs.

Characterizations: XRD patterns were measured using a Bruker D8 Focus X-ray diffractometer with Cu-Kα radiation (1.54056 Å). The morphology was examined using scanning electron microscopy (SEM, FEI Sirion XL30 SEM). TEM was carried out using an FEI Tecnai G2 F20. Raman spectra were obtained on a Renishaw InVia Raman Microscope. TGA measurements were run on a Q50 TGA instrument. Nitrogen adsorption–desorption isotherms were measured using Quantachrome NOVA 4200e system. Samples were degassed at 200 °C for 10 h under vacuum prior to measurements. The Specific surface area and pore size distribution were determined by BET, density functional theory desorption analyses, respectively.

CR 2016 coin-type cells were assembled with metallic lithium anodes for electrochemical measurements. The positive electrodes were fabricated by casting a slurry consisting of as-prepared sample (80 wt%), Super P carbon black (10 wt%), and poly(vinylidene fluoride) (10 wt%) dispersed in *N*-methyl-2-pyrrolidone onto a copper foil with a doctor blade, followed by drying at 80 °C under vacuum overnight. Electrodes were punched into discs with diameter of 8 mm, and the active material loading on every electrode was about 0.3–0.5 mg. Electrolyte we used was obtained from MTI Co. (Item No.: EQ-Be-LiPF6), which was 1 M $LiPF_6$ in 1:1:1 ethylene carbonate/ethyl methyl carbonate/dimethyl carbonate. The cells were assembled in an Ar-filled glove box (Braun) with O_2 and H_2O lower than 0.5 ppm.

Supporting Information

Supporting Information is available from the Wiley Online Library or from the author.

[1] R. C. Massé, E. Uchaker, G. Cao, *Sci. China Mater.* **2015**, *58*, 715.

[2] E. Uchaker, G. Cao, *Nano Today* **2014**, *9*, 499.

[3] a) J. B. Goodenough, K.-S. Park, *J. Am. Chem. Soc.* **2013**, *135*, 1167; b) T.-H. Kim, J.-S. Park, S. K. Chang, S. Choi, J. H. Ryu, H.-K. Song, *Adv. Energy Mater.* **2012**, *2*, 860.

[4] Q. Zhang, E. Uchaker, S. L. Candelaria, G. Cao, *Chem. Soc. Rev.* **2013**, *42*, 3127.

[5] a) M. M. Thackeray, C. Wolverton, E. D. Isaacs, *Energy Environ. Sci.* **2012**, *5*, 7854; b) J. Liu, J.-G. Zhang, Z. Yang, J. P. Lemmon, C. Imhoff, G. L. Graff, L. Li, J. Hu, C. Wang, J. Xiao, G. Xia, V. V. Viswanathan, S. Baskaran, V. Sprenkle, X. Li, Y. Shao, B. Schwenzer, *Adv. Funct. Mater.* **2013**, *23*, 929.

[6] a) J. Qin, C. He, N. Zhao, Z. Wang, C. Shi, E. Z. Liu, J. Li, *ACS Nano* **2014**, *8*, 1728; b) Z. Wang, Z. Wang, W. Liu, W. Xiao, X. W. Lou, *Energy Environ. Sci.* **2013**, *6*, 87.

[7] a) K. Cao, L. Jiao, H. Xu, H. Liu, H. Kang, Y. Zhao, Y. Liu, Y. Wang, H. Yuan, *Adv. Sci.* **2015**, DOI 10.1002/advs.201500185; b) K. Cao, L. Jiao, Y. Liu, H. Liu, Y. Wang, H. Yuan, *Adv. Funct. Mater.* **2015**, *25*, 1082; c) K. Cao, L. Jiao, H. Liu, Y. Liu, Y. Wang, Z. Guo, H. Yuan, *Adv. Energy Mater.* **2015**, *5*, 1401421.

[8] N. Yesibolati, M. Shahid, W. Chen, M. N. Hedhili, M. C. Reuter, F. M. Ross, H. N. Alshareef, *Small* **2014**, *10*, 2849.

[9] X. M. Yin, C. C. Li, M. Zhang, Q. Y. Hao, S. Liu, L. B. Chen, T. H. Wang, *J. Phys. Chem. C* **2010**, *114*, 8084.

[10] H.-X. Zhang, C. Feng, Y.-C. Zhai, K.-L. Jiang, Q.-Q. Li, S.-S. Fan, *Adv. Mater.* **2009**, *21*, 2299.

[11] S.-M. Paek, E. Yoo, I. Honma, *Nano Lett.* **2009**, *9*, 72.

[12] X. W. Lou, C. M. Li, L. A. Archer, *Adv. Mater.* **2009**, *21*, 2536.

[13] M.-S. Park, G.-X. Wang, Y.-M. Kang, D. Wexler, S.-X. Dou, H.-K. Liu, *Angew. Chem. Int. Ed.* **2007**, *46*, 750.

[14] J. Liang, X.-Y. Yu, H. Zhou, H. B. Wu, S. Ding, X. W. D. Lou, *Angew. Chem. Int. Ed.* **2014**, *53*, 12803.

[15] a) M. Zhang, D. Lei, Z. Du, X. Yin, L. Chen, Q. Li, Y. Wang, T. Wang, *J. Mater. Chem.* **2011**, *21*, 1673; b) X. Wang, X. Zhou, K. Yao, J. Zhang, Z. Liu, *Carbon* **2011**, *49*, 133.

[16] J. Wang, W. Li, F. Wang, Y. Xia, A. M. Asiri, D. Zhao, *Nanoscale* **2014**, *6*, 3217.

[17] X. W. Lou, J. S. Chen, P. Chen, L. A. Archer, *Chem. Mater.* **2009**, *21*, 2868.

[18] X. W. Lou, Y. Wang, C. Yuan, J. Y. Lee, L. A. Archer, *Adv. Mater.* **2006**, *18*, 2325.

[19] S. Han, B. Jang, T. Kim, S. M. Oh, T. Hyeon, *Adv. Funct. Mater.* **2005**, *15*, 1845.

[20] J. Fan, T. Wang, C. Yu, B. Tu, Z. Jiang, D. Zhao, *Adv. Mater.* **2004**, *16*, 1432.

[21] Y. Wang, D. Su, C. Wang, G. Wang, *Electrochem. Commun.* **2013**, *29*, 8.

[22] W. Stöber, A. Fink, E. Bohn, *J. Colloid Interface Sci.* **1968**, *26*, 62.

[23] J. G. Kim, S. H. Lee, S. H. Nam, S. M. Choi, W. B. Kim, *RSC Adv.* **2012**, *2*, 7829.

[24] Q. Tian, Y. Tian, Z. Zhang, L. Yang, S.-I. Hirano, *J. Power Sources* **2014**, *269*, 479.

[25] Y. Liu, N. Zhang, L. Jiao, Z. Tao, J. Chen, *Adv. Funct. Mater.* **2015**, *25*, 214.

[26] J. Li, P. Wu, Y. Ye, H. Wang, Y. Zhou, Y. Tang, T. Lu, *CrystEngComm* **2014**, *16*, 517.

[27] G. Zhou, D.-W. Wang, L. Li, N. Li, F. Li, H.-M. Cheng, *Nanoscale* **2013**, *5*, 1576.

[28] P. Poizot, S. Laruelle, S. Grugeon, L. Dupont, J.-M. Tarascon, *Nature* **2000**, *407*, 496.

[29] a) M. Zhang, T. Wang, G. Cao, *Int. Mater. Rev.* **2015**, *60*, 330; b) M. Gao, X. Chen, H. Pan, L. Xiang, F. Wu, Y. Liu, *Electrochim. Acta* **2010**, *55*, 9067.

[30] F. Wang, X. Song, G. Yao, M. Zhao, R. Liu, M. Xu, Z. Sun, *Scr. Mater.* **2012**, *66*, 562.

[31] R. Demir-Cakan, Y.-S. Hu, M. Antonietti, J. Maier, M.-M. Titirici, *Chem. Mater.* **2008**, *20*, 1227.

[32] C. Xu, J. Sun, L. Gao, *J. Mater. Chem.* **2012**, *22*, 975.

[33] X. Zhu, Y. Zhu, S. Murali, M. D. Stoller, R. S. Ruoff, *J. Power Sources* **2011**, *196*, 6473.

[34] S. M. Lee, S. H. Choi, Y. C. Kang, *Chem. Eur. J.* **2014**, *20*, 15203.

[35] S. R. Mukai, T. Hasegawa, M. Takagi, H. Tamon, *Carbon* **2004**, *42*, 837.

[36] X. Zhou, W. Liu, X. Yu, Y. Liu, Y. Fang, S. Klankowski, Y. Yang, J. E. Brown, J. Li, *ACS Appl. Mater. Interfaces* **2014**, *6*, 7434.

[37] a) J. Wang, Q. Zhang, X. Li, D. Xu, Z. Wang, H. Guo, K. Zhang, *Nano Energy* **2014**, *6*, 19; b) B. Huang, X. Li, Z. Wang, H. Guo, X. Xiong, J. Wang, *J. Alloys Compd.* **2014**, *583*, 313.

[38] a) J. Zhu, G. Zhang, X. Yu, Q. Li, B. Lu, Z. Xu, *Nano Energy* **2014**, *3*, 80; b) J. Zhu, D. Deng, *J. Phys. Chem. C* **2015**, *119*, 21323.

[39] J. Huang, X. Xu, C. Gu, W. Wang, B. Geng, Y. Sun, J. Liu, *Sens. Actuators, B* **2012**, *173*, 599.